Universal Solution Synthesis of Sulfide Solid Electrolytes Using Alkahest for All-Solid-State Batteries

Ji Eun Lee, Kern-Ho Park, Jin Chul Kim, Tae-Ung Wi, A. Reum Ha, Yong Bae Song, Dae Yang Oh, Jehoon Woo, Seong Hyeon Kweon, Su Jeong Yeom, Woosuk Cho, KyungSu Kim, Hyun-Wook Lee,* Sang Kyu Kwak,* and Yoon Seok Jung*

The wet-chemical processability of sulfide solid electrolytes (SEs) provides intriguing opportunities for all-solid-state batteries. Thus far, sulfide SEs are wet-prepared either from solid precursors suspended in solvents (suspension synthesis) or from homogeneous solutions using SEs (solution process) with restricted composition spaces. Here, a universal solution synthesis method for preparing sulfide SEs from precursors, not only Li_2S, P_2S_5, LiCl, and Na_2S, but also metal sulfides (e.g., GeS_2 and SnS_2), fully dissolved in an alkahest: a mixture solvent of 1,2-ethylenediamine (EDA) and 1,2-ethanedithiol (EDT) (or ethanethiol). Raman spectroscopy and theoretical calculations reveal that the exceptional dissolving power of EDA–EDT toward GeS_2 is due to the nucleophilicity of the thiolate anions that is strong enough to dissociate the Ge—S bonds. Solution-synthesized $Li_{10}GeP_2S_{12}$, Li_6PS_5Cl, and $Na_{11}Sn_2PS_{12}$ exhibit high ionic conductivities (0.74, 1.3, and 0.10 mS cm^{-1} at 30 °C, respectively), and their application for all-solid-state batteries is successfully demonstrated.

1. Introduction

The solution processing of metal chalcogenides is key to various electronic- and energy-related devices.[1] All-solid-state batteries (ASSBs) modified to achieve better safety and higher energy density have been emerging for application in battery-driven electric vehicles.[2] Owing to their high ionic conductivities that reach a maximum of $\approx 10^{-2}$ S cm^{-1} at room temperature (e.g., $Li_{10}GeP_2S_{12}$ (LGPS):[3] 12 mS cm^{-1} and $Li_{5.5}PS_{4.5}Cl_{1.5}$:[4] 9.4 mS cm^{-1}) and mechanical deformability that eases the

J. E. Lee, A. R. Ha, Y. B. Song, D. Y. Oh, J. Woo, Y. S. Jung
Department of Chemical and Biomolecular Engineering
Yonsei University
Seoul 03722, South Korea
E-mail: yoonsjung@yonsei.ac.kr
K.-H. Park, W. Cho, K. Kim
Advanced Battery Research Center
Korea Electronics Technology Institute
Seongnam 13509, South Korea
J. C. Kim, T.-U. Wi, S. H. Kweon, S. J. Yeom, H.-W. Lee, S. K. Kwak
School of Energy and Chemical Engineering
Ulsan National Institute of Science and Technology (UNIST)
Ulsan 44919, South Korea
E-mail: hyunwooklee@unist.ac.kr; skkwak@unist.ac.kr

integration to devices, sulfide superionic conductors hold great promise for practical ASSB technologies.[2a,c,j,3–5] Notably, several sulfide solid electrolyte (SE) materials can be synthesized or processed via soft chemistry using liquid solvents, which has become a popular topic in ASSB research.[6]

The "wet" preparation for sulfide SEs is classified into three categories (Figure S1, Supporting Information):[6] i) suspension synthesis, ii) solution process, and iii) solution synthesis. In suspension synthesis, SE precursors are partly dissolved in organic solvents (e.g., tetrahydrofuran and acetonitrile) and the reaction proceeds via a suspension state, with organic solvents serving as a medium for soft chemistry.[7] Compared to conventional solid-state synthesis, the suspension synthesis of sulfide SEs has multiple advantages, such as a reduced reaction time and scalable production of SEs or electrodes.[6b,8] In the solution process, the sulfide SEs, not precursors, are dissolved in specific polar solvents, forming a homogeneous solution. Original SEs can be precipitated via the removal of solvents and subsequent heat treatment (HT). The liquefied sulfide SEs for the solution process can be utilized for coating on active materials[9] and the infiltration of porous composite electrodes or separators.[9a,10] In addition, in situ formation of nanocomposite electrodes via solution processing has been reported.[8b,11] All these methods have demonstrated exceptional advantages in forming intimate ionic contacts and alternative production capability of ASSBs.

Solution synthesis, in which SE precursors are fully dissolved in solvents and SEs are formed via the removal of solvents, could be ideal because it combines the advantages of both the solution process (i.e., forming a homogeneous solution) and suspension synthesis (i.e., using SE precursors). However, solvents that are known to form homogeneous SE solutions (e.g., ethanol (EtOH) and water) are highly polar and protic, and they readily hydrolyze P_2S_5 and/or Li_2S precursors.[6a] This explains the limited types of solution-processable SEs, such as (LiI-)Li_4SnS_4 using methanol (MeOH) or water,[9a] Li_6PS_5Cl (LPSCl) using EtOH,[9c,10] and Na_3SbS_4 using MeOH or water.[9b] To date, only a few solution syntheses for sulfide SEs have been identified.[12] Notably, all suspension and solution syntheses of SEs thus far have covered only restricted compositions, those based on binary (Li_2S–P_2S_5) or ternary systems (Li_2S–P_2S_5–LiX),

and excluded metal sulfides such as GeS$_2$ (Table S1, Supporting Information). This is attributed to the limited dissolving power of the solvents used for the suspension synthesis. Thus, the counteracting requirement of solvents for solution synthesis, i.e., high dissolving power for homogeneous solutions but inertness toward vulnerable sulfide precursors, has been a formidable challenge.

Here, we demonstrate the first universal solution synthesis of sulfide SEs using an alkahest solvent system. Binary mixtures of 1,2-ethylenediamine (EDA)–1,2-ethanedithiol (EDT) and EDA–ethanethiol (ET), which show strong dissolving power for metal chalcogenides, fully dissolved not only conventional sulfide SE precursors of Li$_2$S, P$_2$S$_5$, LiCl, and Na$_2$S, but also metal sulfides, such as GeS$_2$ and SnS$_2$. The dissolution mechanism of GeS$_2$ in EDA–EDT solvents was revealed using density functional theory calculations. The dissolution of precursors in the EDA–EDT solvents, followed by precipitation via the removal of solvents, and subsequent HT, yielded the targeted SEs, LGPS, LPSCl, and Na$_{11}$Sn$_2$PS$_{12}$ (NSPS) with high ionic conductivities (0.74, 1.3, and 0.10 mS cm^{-1}, respectively). Furthermore, their applicability for ASSBs employing TiS$_2$ and Na$_2$S/carbon nanocomposites was demonstrated.

2. Results and Discussions

Binary solvent mixtures of EDA–EDT with various volume fractions (0%, 20%, 40%, and 100% EDT) were prepared and their molecular interactions were examined using Raman spectroscopy (**Figure 1**a). For pure EDT (EDA:EDT = 0:100 vol), the distinct peaks at 2555 and 817 cm^{-1} are attributed to S–H stretching and C–S–H bending modes, respectively, indicating the presence of the thiol group.[13] Upon addition of 60 vol% of EDA, the intensities of the peaks of the thiol group for EDT were reduced by >90%. This result indicates the significant deprotonation of EDT and the resulting generation of thiolate anions (EDT^{2-}), which should be accompanied by the protonation of EDA. Compared with the spectrum of pure EDA, the N–H stretching peak at 3298 cm^{-1} underwent a red shift upon the addition of EDT. This result confirms the protonation of EDA, where the N–H bonds are slightly elongated.[14]

The dissolving ability of the EDA–EDT solvent (10:1 vol) was assessed for the major SE precursors that were used for conventional compositions of Li$_2$S–P$_2$S$_5$(–LiX) or Na$_2$S–P$_2$S$_5$(–NaX) (Figure 1b). All precursors of Li$_2$S, P$_2$S$_5$, LiCl, and Na$_2$S were fully dissolved in EDA–EDT without any side reactions. Specifically, the full dissolution of P$_2$S$_5$ and Li$_2$S into EDA–EDT is noteworthy, which is in sharp contrast to the hydrolysis of P$_2$S$_5$ by EtOH and incomplete dissolution of Li$_2$S in anhydrous EtOH, respectively.[15] More importantly, the EDA–EDT solvent exhibited exceptional dissolving ability for the unprecedented SE precursor for the wet-chemical synthesis of sulfide SEs, GeS$_2$ (Figure 1c). Pure EDA could not dissolve GeS$_2$, which is similar to conventional protic solvents, such as water, EtOH, and MeOH. GeS$_2$ in pure EDA remained in a dark suspension, even after a day. In sharp contrast, the EDA–EDT solvent fully dissolved GeS$_2$ within seconds and showed a transparent pinkish solution (Figure 1c). The UV–vis spectrum of the GeS$_2$/(EDA–EDT) solution confirmed the absence of light

scattering by solid particulates of >1 nm (Figure S2, Supporting Information).[16] Furthermore, SnS$_2$ could be dissolved in EDA–EDT, forming a clear yellowish solution (Figure 1d) after gentle heating at 60 °C. With varying the EDA/EDT ratio, the dissolving ability of EDA–EDT for each SE precursor was assessed (Table S2, Supporting Information). The solvent mixture was solidified when the volume fraction of EDT was higher than 10:4 (EDA/EDT).[14] The solubility limits of Li$_2$S, P$_2$S$_5$, LiCl, GeS$_2$, and Na$_2$S for EDA–EDT with 10:1 vol were 1.31, 1.65, 1.41, 0.82, and 0.59 M, respectively, and the solubility limits for Li$_2$S and GeS$_2$ slightly decreased to 1.09 and 0.51 M for EDA–EDT with 10:3 vol.

The dissolution mechanism of GeS$_2$ in EDA–EDT was examined using Raman spectroscopy (Figure 1e). For the GeS$_2$/(EDA–EDT) solution, the peak at 410 cm^{-1} indicates the evolution of the sulfur-terminating Ge–S$^-$ bonding,[17] which is absent for GeS$_2$ powders (Figure S3, Supporting Information). This observation suggests that the Ge–S bonds in solid GeS$_2$ were broken via nucleophilic thiolate anions and dissociated into molecular solutes (Figure S4, Supporting Information). Considering the strong Ge–S–Ge signal at 356 cm^{-1}, the solute is a polyanionic species.[17] Moreover, as GeS$_2$ was dissolved in EDA–EDT, the peak intensities for the C–S bonding (651, 678, and 732 cm^{-1}) were slightly reduced, while that for the N–H stretching mode (3298 cm^{-1}) remained unchanged (Figure 1e). This result reflects the change in the chemical environments near the thiolate anions due to the dissolution of GeS$_2$. The absence of disulfide bonding (v_{S-S} = 510 and 524 cm^{-1})[18] for the GeS$_2$/(EDA–EDT) solution suggests that thiolate anions were bonded to Ge ions rather than sulfur atoms for GeS$_2$ (Figure 1e). Based on this understanding, the new Raman peak that evolved near 651 cm^{-1} was tentatively assigned to C–S–Ge bonding (inset (right) in Figure 1e).

We examined the proton transfer in the EDA–EDT mixture solution and the dissolution mechanism of GeS$_2$ in EDA–EDT using theoretical calculations (see theoretical calculations in the Experimental Section). The EDA–EDT (10:1 vol) mixture solvent modeled using molecular dynamics simulation was used to check the probability of proton transfer in the mixture solution. The proton transfer energy from EDT to EDA in molecules within 3 Å around the EDT in the relaxed solvent structure was calculated to be –0.61 eV through density functional theory calculations (Figure S5, Supporting Information). From these results, we revealed that the thiolate anion could be readily formed via proton transfer from EDT to EDA. In addition, the molecular electrostatic potential map reveals that the deprotonated EDT has the point of nucleophilic attack, which is the deprotonated thiolate anion (Figure S6, Supporting Information).[19] Furthermore, to elucidate the mechanism of the dissolution reaction of the GeS$_2$ crystal, we traced the step-by-step pathway in dissociating the Ge–S bond in the GeS$_2$ surface caused by thiolate anions (Figure 2; Figures S7 and S8, Supporting Information). The pathway of GeS$_2$ dissolution was assumed to gradually dissociate the Ge–S bond in GeS$_2$ via the nucleophilic attack of thiolate anions. It should be noted that in the first step, the thiolate anion was adsorbed on the uncoordinated Ge site (G$_1$ site) on the GeS$_2$ surface, and the Ge–S bond on the GeS$_2$ surface was dissociated with no activation energy (E_a), indicating that the thiolate anion is a strong nucleophilic
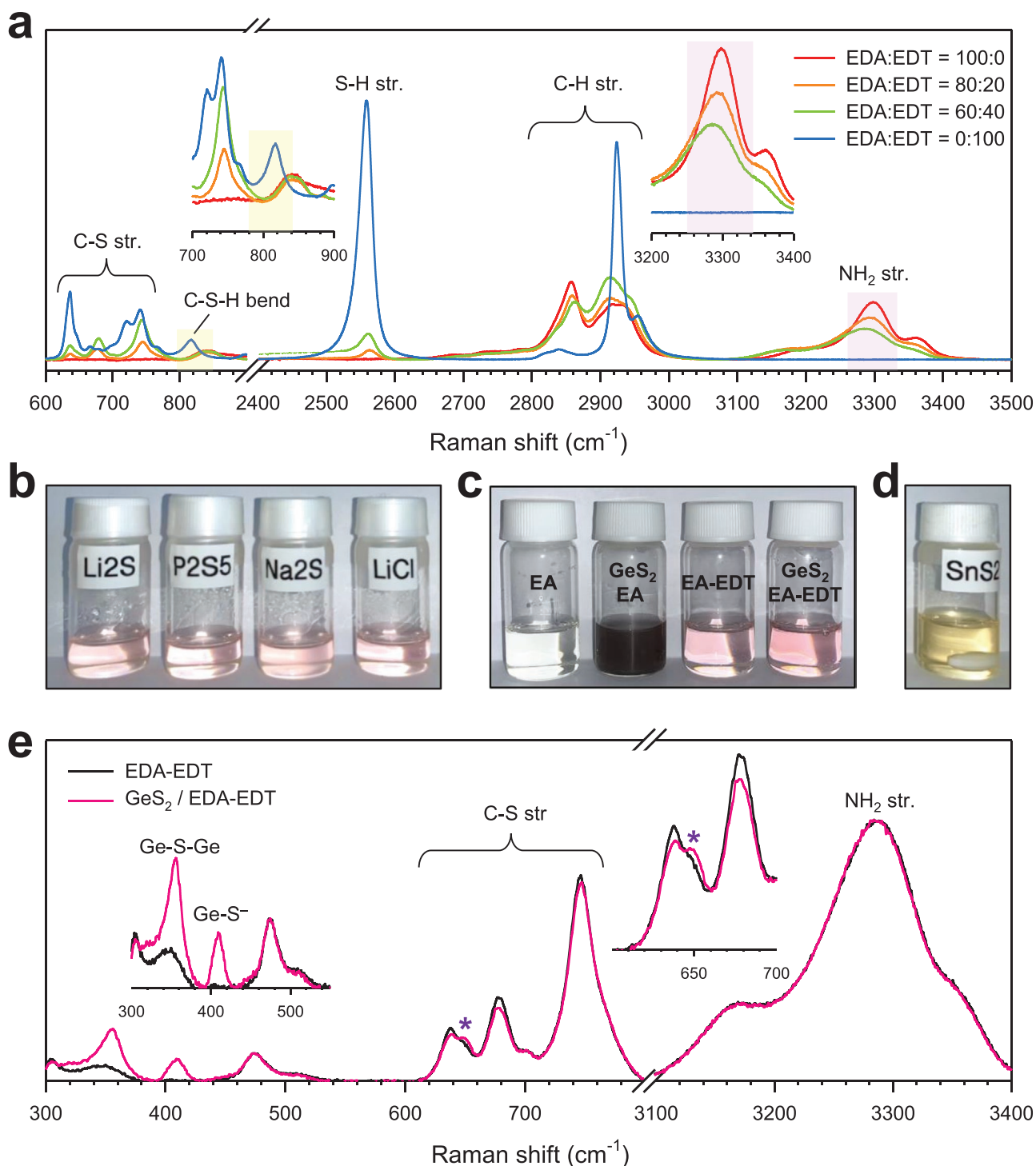
Figure 1. Results of the dissolution of sulfide SE precursors in EDA–EDT cosolvents. a) Raman spectra of EDA–EDT cosolvents with varying volume ratio. The insets show enlarged views of the C–S–H bending peaks (highlighted in yellow) and NH_2 stretching peaks (highlighted in pink). b) Photograph of SE precursors, Li_2S, P_2S_5, Na_2S, LiCl, in EDA–EDT. c) Photograph of GeS_2 in EDA and EDA–EDT. d) Photograph of SnS_2 in EDA–EDT. e) Raman spectra for the solution of GeS_2 dissolved in the EDA–EDT cosolvent, showing the signals of Ge–S$^-$ and Ge–S–Ge (inset), in comparison with that for the EDA–EDT cosolvent. The inset in the right shows an enlarged view of the C–S stretching peaks and unknown peak (denoted as "*").

attacker capable of separating Ge–S bonds (i.e., from IS to IS_{ad}). In the subsequent reaction, the additional deprotonated EDT was continuously attached to the Ge site exposed on the surface, dissociating the bond between Ge and sulfur on the surface. Finally, the product was a (thiolate)$_2$–G$_1$–S$_2$–G$_2$–S$_2$–G$_3$–(thiolate)$_2$ structure and completely dissolved from the GeS_2 surface. Importantly, the total GeS_2 dissolution mechanism via the nucleophilic attack of the thiolate anion requires a low

**ADVANCED
SCIENCE NEWS**

www.advancedsciencenews.com

**ADVANCED
MATERIALS**
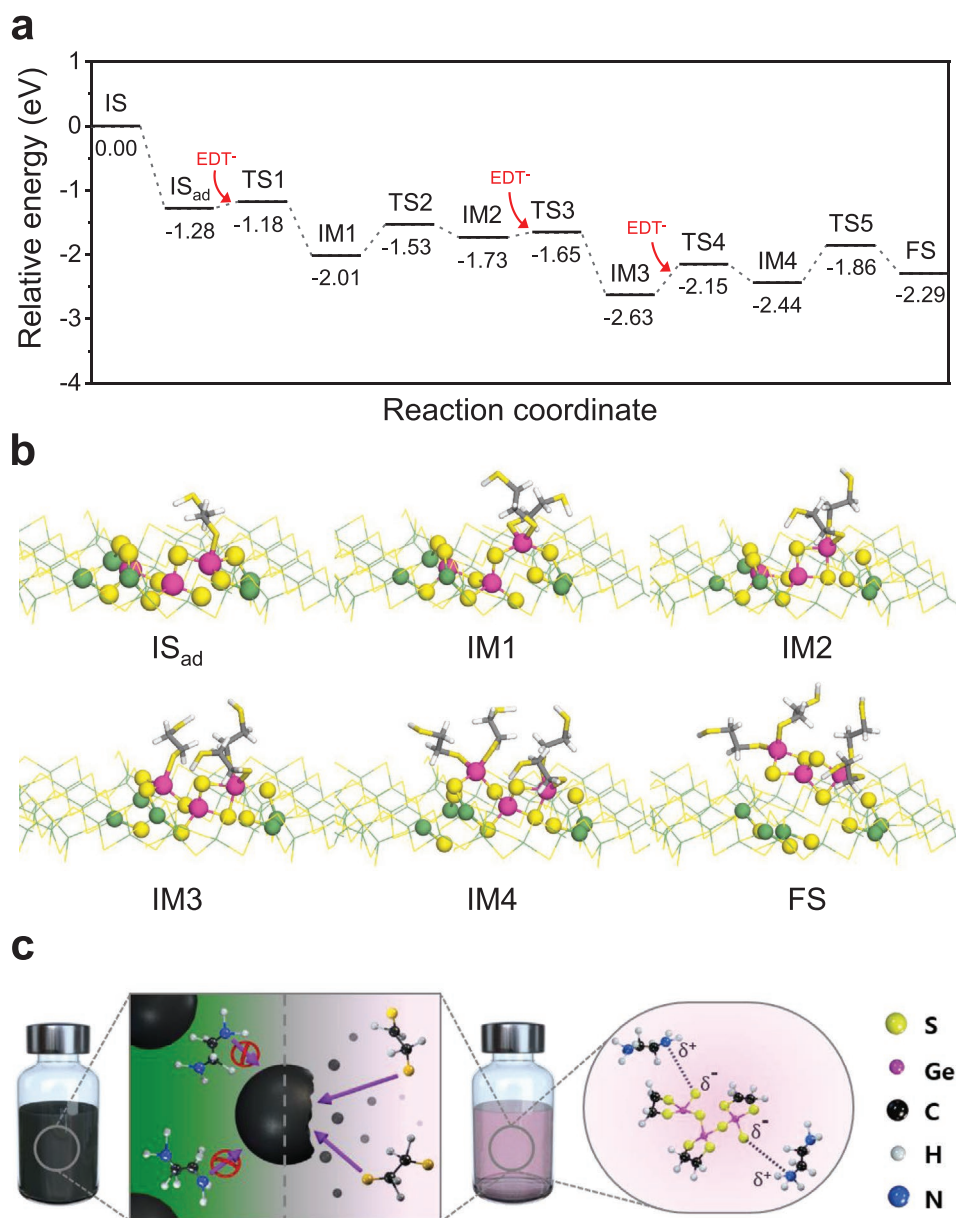
www.advmat.de

a

b

c

Figure 2. Dissolution mechanism of sulfide SE precursors in EDA–EDT cosolvents. a) Reaction coordinates of dissolution mechanism of the GeS$_2$ surface. b) Magnified view of the optimized configurations of each state. In (b), IS, IM, TS, and FS in each reaction mechanism represent initial state, intermediate, transition state, and final state, respectively. For the clear view, the dissolved Ge atoms and surface atoms near the Ge atoms are depicted using the ball-and-stick model, and the deprotonated EDT molecules are depicted using the stick model. The remaining atoms are indicated as lines. The dissolved three Ge atoms are colored pink and the remaining Ge, C, S, N, H atoms are colored green, gray, yellow, blue, and white, respectively. A detailed explanation is provided in the Supporting Information. c) A schematic showing the dissolution mechanism of GeS$_2$ in EDA–EDT cosolvents.

activation energy, indicating that the Ge—S cluster could be easily formed. This mechanistic calculation suggested a plausible formation of polyanionic Ge—S clusters through a continuous dissolution reaction. Likewise, the dissociation of P$_2$S$_5$, Li$_2$S, and Na$_2$S by EDT$^-$ were also favorable (Figures S9–S11, Supporting Information)

Overall, Raman spectroscopy and theoretical calculation results collectively suggest that the thiolate anions dissociate GeS$_2$ crystals into Ge—S ionic fragments via nucleophilic attack, and the EDT^{2-}-terminated polyanionic species are then counterbalanced by the protonated EDA cation (**Figure 2**c).

Three representative sulfide SEs, LGPS, LPSCl, and NSPS, were selected as test vehicles to validate the universal feasibility of solution synthesis using EDA–EDT, and the results are displayed in **Figure 3**. The relevant precursors were dissolved in EDA–EDT to form transparent homogeneous solutions, which was followed by the removal of solvents and subsequent HT (Figure S12, Supporting Information). Field-emission scanning electron microscopy images of the solution-synthesized SEs are shown in Figure S13 of the Supporting Information. For all the SEs obtained via the solution synthesis using EDA–EDT (referred to as "EDT-SEs"), main reflections for the
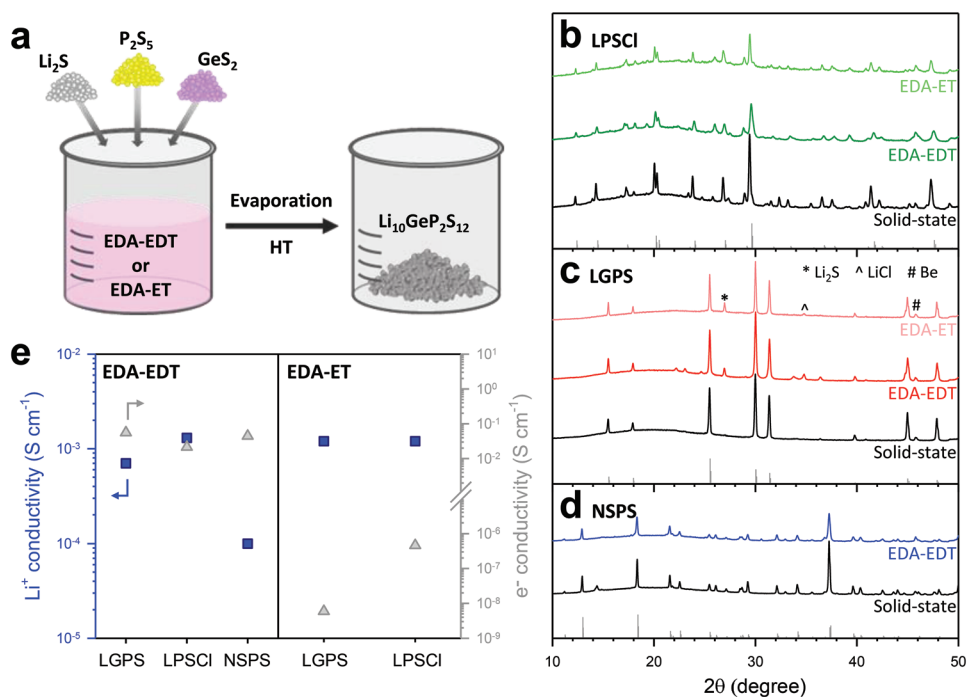
Figure 3. Solution synthesis of sulfide SEs using EDA–EDT and EDA–ET. a) Schematic illustrating solution synthesis of LGPS ($Li_{10}GeP_2S_{12}$). XRD patterns of b) LGPS, c) LPSCl (Li_6PS_5Cl), and d) NSPS ($Na_{11}Sn_2PS_{12}$)[20] prepared via solution versus solid-state synthesis. Bragg peaks for $Li_{10}GeP_2S_{12}$ (ICSD no. 425992), Li_6PS_5Cl (ICSD no. 418490), and $Na_{11}Sn_2PS_{12}$ are also shown at the bottom of each panel. e) Li^+ and e^- conductivities at 30 °C for EDT- and ET-SEs.

powder X-ray diffraction (XRD) patterns were identical to those for the samples prepared via conventional solid-state reaction (Figure 3b–d). Notably, the electronic conductivities for EDT-LGPS, EDT-LPSCl, and EDT-NSPS were significant: 17, 19, and 13 mS cm^{-1}, respectively (Figure 3e; Figure S14, Supporting Information). This result is attributed to the residual solvent carbonized upon HT, which will be discussed later. Thus, the EDT-SE samples were subjected to electrochemical impedance spectroscopy measurements using Ti/Li/LPSX/(EDT-SE)/LPSX/Li/Ti symmetric cells to extract the ionic conductivities (see the Experimental Section and Figure S15, Supporting Information). The ionic conductivities of 0.74, 1.3, and 0.10 mS cm^{-1} at 30 °C were obtained for LGPS, LPSCl, and NSPS, respectively (Figure 3e). Notably, these values approached those for samples produced via conventional solid-state synthesis (7.0, 3.5, and 1.0 mS cm^{-1} for LGPS, LPSCl, and NSPS, respectively (cold-pressed pellet)).[3,4,20] More importantly, the solution synthesis process for the three SEs is unprecedented. Furthermore, the ionic conductivities of 0.74 and 1.3 mS cm^{-1} for EDT-LGPS and EDT-LPSCl, respectively, are at the highest level, compared with materials prepared via the solution process (Table S1, Supporting Information). The slightly lower ionic conductivities for EDT-SEs, compared to those for the samples produced via conventional solid-state synthesis, are attributed to the presence of residual carbon, which interrupts Li$^+$ migration.[21]

Thermogravimetric analysis (TGA) and Raman spectroscopy measurements were carried out to trace the structural construction of SEs and residual carbon for EDT-SEs. Raman analysis was conducted on the EDT-LPSCl samples heat-treated at different temperatures (**Figure 4a**). The powders heat-treated

at 150 °C showed a peak for PS_4^{3-} at 420 cm^{-1} without any signals for unreacted precursors,[9a] indicating that the structural frameworks of sulfide SEs were already formed from the dissociated precursors. In addition, distinct peaks at 3070–2760 cm^{-1} (denoted "#") and 3340–3240 cm^{-1} (denoted "^"), attributed to C−H and N−H stretching, respectively, indicate residual organic species. Increasing the HT temperature to 350, 550, and 700 °C led to the evolution of D- and G-bands in the range of 1580–1350 cm^{-1}, which confirms the carbonization of the organic residues.[22] The TGA profile showed that most of the solvents were removed by 300 °C (Figure S16, Supporting Information).[14] However, a further decrease in weight loss in the range of 290–350 °C reflects the carbonization of residual solvents. Indeed, the weight fraction of carbon in the EDT-LPSCl samples, determined through elemental analysis, was 2.03% (Table S3, Supporting Information). The incomplete removal of solvents for the EDT-SEs could be due to the high boiling point of EDT (146 °C) and the strong chemical interaction between EDA–EDT and SE precursor molecules.

To minimize the amount of residual solvents that are subjected to carbonization, solution synthesis using an alternative solvent, EDA-ET (b.p. of ET = 35 °C), was carried out. EDA–ET (10:2 vol) could also fully dissolve each SE precursor (Figure S17, Supporting Information). After evaporation of the solvent and subsequent HT at 550 °C, SEs with targeted compositions (denoted as "ET-SEs") were obtained (Figure 3b–d), only except for ET-NSPS (Figure S18, Supporting Information). The ionic and electronic conductivities are summarized in Table S4 of the Supporting Information, and the Arrhenius plots for the ionic conductivity are shown in Figure S19 of the Supporting
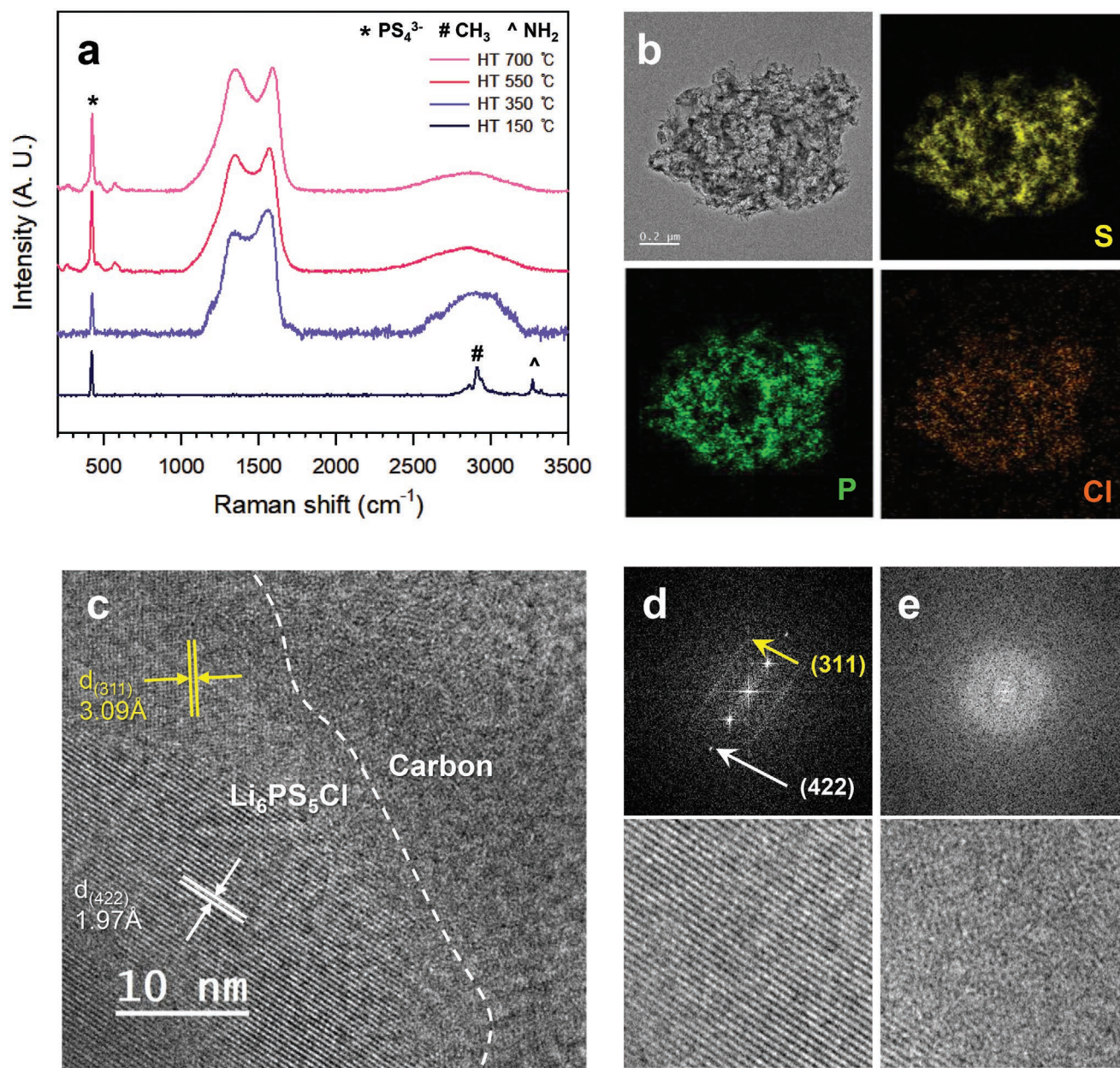
Figure 4. Characterization of Li_6PS_5Cl prepared using EDA–EDT. a) Raman spectra for EDT-LPSCl prepared at different HT temperatures. b) Cryo-TEM image of EDT-LPSCl and corresponding elemental maps for sulfur, phosphorus, and chlorine. Cryo-TEM images of EDT-LPSCl at c) lower magnification and d,e) higher magnification with corresponding inverse-fast Fourier transform (FFT) patterns.

Information. The LGPS and LPSCl prepared using EDA–ET (ET-LGPS and ET-LPSCl, respectively) showed high ionic conductivities of 1.2 mS cm^{-1} (Table S4, Supporting Information). Notably, ET-SEs prepared at 550 °C showed much lower electronic conductivities (ET-LGPS: 5.9×10^{-9} S cm^{-1}, ET-LPSCl: 4.6×10^{-7} S cm^{-1}) than those obtained using EDA–EDT (e.g., EDT-LPSCl prepared at 550 °C: 1.7×10^{-5} S cm^{-1}), reflecting much lowered amounts of carbon. This result emphasizes the importance of solvent design to control the amount of residual carbons in solution-synthesized SEs. Increasing the amount of carbon residue accelerates the electrochemical decomposition of solution-synthesized SEs. From the cyclic voltammetry tests

using SE/ss-LPSCl/Li-In cells, EDT-SEs with higher electronic conductivities (thus, more residual carbons) showed the higher redox currents compare to ET-SEs (Figure S20, Supporting Information).

Nanostructures of EDT-LPSCl were further probed via cryogenic transmission electron microscopy (cryo-TEM) measurements to suppress any phase changes induced by a strong electron beam (Figure 4b–e; Figure S21, Supporting Information).[23] Energy dispersive X-ray spectroscopy (EDXS) maps for EDT-LPSCl denote the even distribution of C 1s signals throughout the SE particles (Figure S21, Supporting Information). It is shown that the crystalline and amorphous regions

are distributed at the nanoscale (Figure 4c). The lattice spacing for the crystalline domain was determined to be 0.20 nm, which corresponds to the (422) plane of Li_6PS_5Cl (Figure 4d). The amorphous domain corresponding to carbon (Figure 4e) was found around the crystalline Li_6PS_5Cl. Similar results for the nanodomains of SEs and carbon were also obtained for the EDT-LGPS, ET-LPSCl, and ET-LGPS samples (Figure S22, Supporting Information).

The electrochemical performance of TiS_2/Li-In cells at 30 °C for using solution-synthesized SEs as the catholyte and/or separating SE layer is shown in Figure 5, and Figures S23 and S23 (Supporting Information). When EDT-SEs were used as the SE layer, corresponding cells exhibited open-circuit voltages decreasing over time and reaching to 0 V, which is an indicative of the significant electrical leakages (Figure S25, Supporting Information). Thus, SEs prepared by solid-state reaction (denoted as "ss-SEs") were used as the SE layer. TiS_2 cells employing EDT-LPSCl, EDT-LGPS, and EDT-NSPS as the catholyte showed reversible capacities of 231, 258, and 199 mA h g^{-1} and excellent capacity retention over 100 cycles (**Figure 5**), confirming that the presence of residual carbon did not decrease the potential of the EDT-SEs for use in composite electrodes. On the other hand, ET-SEs showing low electronic conductivities could be employed as the SE layer. TiS_2/Li-In cells employing ET-LPSCl and ET-LGPS as the SE layer exhibited reversible capacities of 223 and 206 mA h g^{-1} with high

initial Coulombic efficiencies of 96.6% and 91.2%, respectively (Figure 5). However, the cells using ET-LPSCl showed abnormally high Coulombic efficiencies of >100% at subsequent cycles, which is in contrast to that for using ET-LGPS (Figure S24, Supporting Information). This result is explained by the difference in electronic conductivity between ET-LPSCl (4.6×10^{-7} S cm^{-1}) and ET-LGPS (5.9×10^{-9} S cm^{-1}).

Exploiting the homogeneous feature of the precursor/(EDA–EDT) solution and the facile formation of carbon networks at the nanoscale via solution synthesis, nanocomposites of Na_2S, NSPS, and carbon were prepared via a one-pot solution synthesis. The addition of Na_2S, P_2S_5, SnS_2, and super C65 to the EDA–EDT solvent (10:1 vol) resulted in carbon particles (super C65) suspended in a homogeneous solution, which was subjected to solvent evaporation and subsequent HT at 700 °C (**Figure 6**a). XRD patterns of the product showed reflections for Na_2S and $Na_{11}Sn_2PS_{12}$ without any impurity phases (Figure 6b). The microstructures of the Na_2S–NSPS–C nanocomposites were also analyzed via cryo-TEM measurements (Figure 6c). Crystalline grains of Na_2S, NSPS, and graphitic carbon with tens of nanometers in size were uniformly distributed. Specifically, the (204) plane of the $Na_{11}Sn_2PS_{12}$ and the (111) plane of Na_2S were identified. Corresponding lattice spacings were determined to be 0.48 and 0.38 nm for $Na_{11}Sn_2PS_{12}$ and Na_2S, respectively (Figure S26, Supporting Information). The uniform distribution of elements at the nanoscale for the Na_2S–NSPS–C
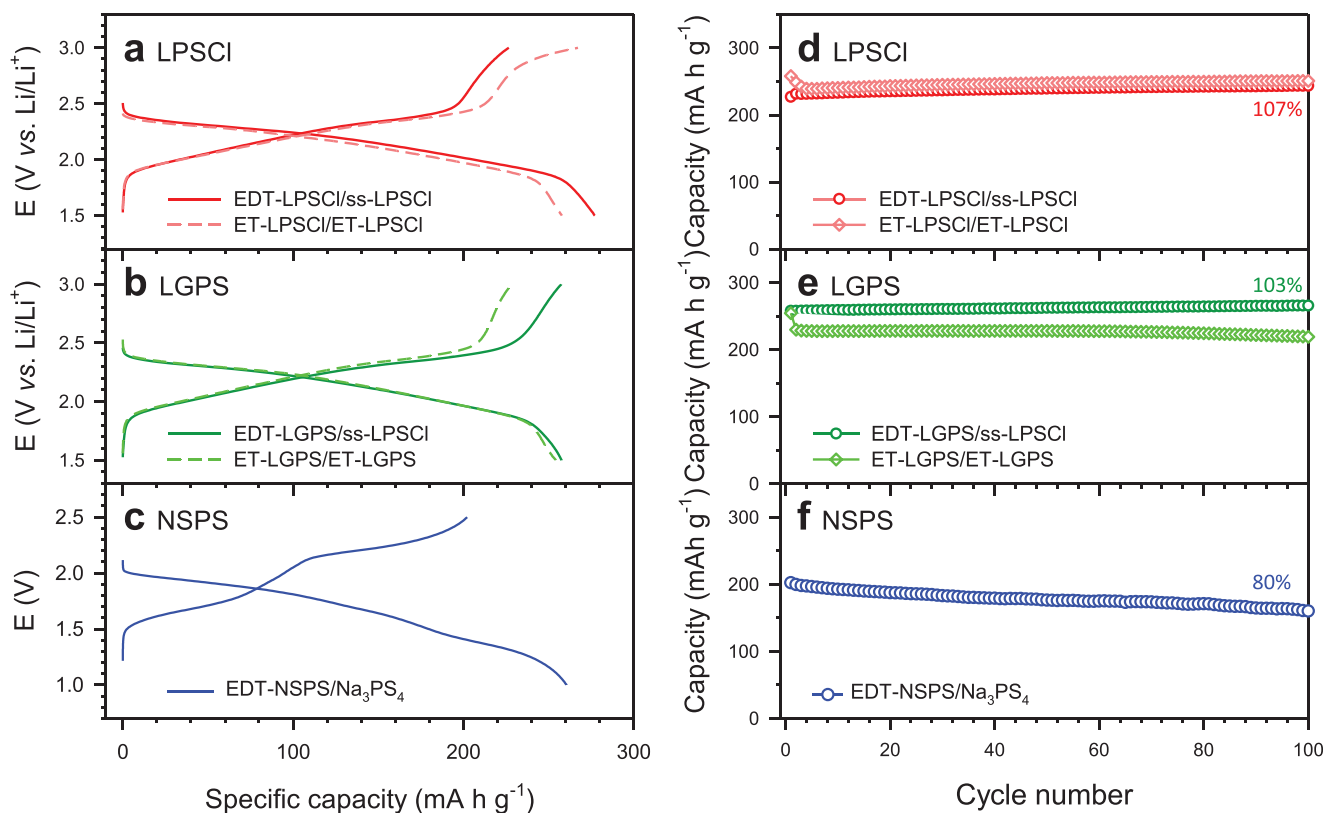

Figure 5. Electrochemical performances at 30 °C for all-solid-state cells using SEs prepared using EDA–EDT and EDA–ET. First-cycle charge–discharge voltage profiles of TiS_2/Li-In cells at 0.3 C for employing solution-synthesized a) LPSCl, b) LGPS, and c) NSPS. d–f) Corresponding cycling performances. SEs used as the catholytes and separating SE layers are denoted as "SE/SE." Full data for using various SEs for catholytes and separating SE layers are shown in Figure S24 of the Supporting Information.

**ADVANCED
SCIENCE NEWS**
www.advancedsciencenews.com

**ADVANCED
MATERIALS**
www.advmat.de

nanocomposites was also confirmed using EDXS elemental maps (Figure 6d). The electrochemical performance at 70 °C of $Na_2S-NSPS-C$ in Na_2S/Na_3Sn all-solid-state cells is presented in Figure 6e, in comparison with the electrodes prepared via manual mixing (Figure 6f). The manually mixed electrodes showed a second discharge capacity of only 147 mA h g^{-1}, and the capacity drastically decayed in the second cycle. In stark contrast, the $Na_2S-NSPS-C$ electrodes exhibited a much higher discharge capacity of 507 mA h g^{-1} (at the second cycle) and moderate capacity retention. The drastic improvement in the cell performance via solution synthesis stems from the

formation of nanosized Na_2S, which is beneficial for shortening conduction pathways and reducing the absolute volume changes upon charge–discharge, and the intimate ionic and electronic contacts enabled by the solution synthesis.[8b,11]

3. Conclusion

In summary, we demonstrated the first universal solution synthesis for sulfide SEs using EDA–EDT and EDA–ET alkahests. The exceptional dissolving power of EDA–EDT for not
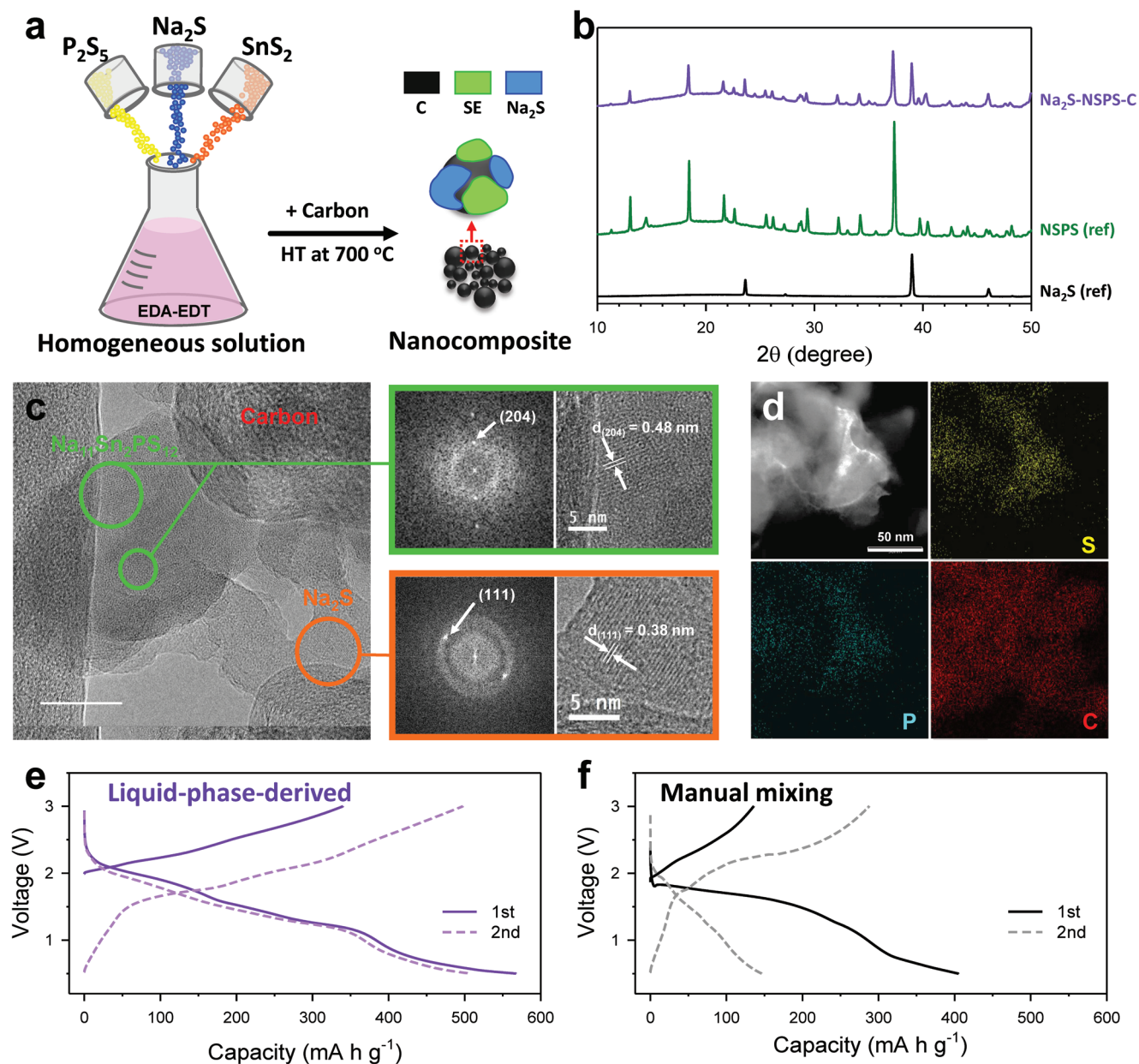

Figure 6. $Na_2S-NSPS-C$ electrodes derived via solution synthesis using EDA–EDT for all-solid-state Na–S batteries. a) Schematic illustrating $Na_2S-NSPS-C$ nanocomposites and b) corresponding XRD pattern. XRD patterns of Na_2S and solid-state synthesized NSPS are also compared. c) Cryo-TEM image for the $Na_2S-NSPS-C$ nanocomposite and corresponding inversed-FFT patterns for the high-magnification regions for $Na_{11}Sn_2PS_{12}$ and Na_2S. d) Dark-field cryo-TEM image for the $Na_2S-NSPS-C$ nanocomposite and corresponding elemental maps. First two-cycle charge–discharge voltage profiles at 70 °C for Na_2S-NSPS-C electrodes prepared via e) solution synthesis and f) manual mixing.

only conventional precursors (Li_2S, P_2S_5, LiX, and Na_2S) but also metal sulfides, such as GeS_2 and SnS_2, and its ability to form homogeneous solutions allowed for the facile synthesis of various classes of sulfide SEs with high ionic conductivities including $Li_{10}GeP_2S_{12}$, Li_6PS_5Cl, and $Na_{11}Sn_2PS_{12}$ (0.74, 1.3, and 0.10 mS cm^{-1} at 30 °C, respectively). The dissolution mechanism of GeS_2 in EDA–EDT was revealed using Raman spectroscopy and DFT calculations. Specifically, the thiolate anions formed in the EDA–EDT solvent system dissociated metal sulfides via nucleophilic attack, forming polyanionic solutes. The applicability of solution-synthesized SEs was successfully demonstrated for TiS_2 electrodes. It was demonstrated that the amount of carbon in the solution-synthesized SEs, originating from organic residue, could be controlled by tuning the chemistry (e.g., using low-b.p. ET) and/or engineering. TiS_2 electrodes employing solution-synthesized SEs exhibited high reversible capacities and stable cycling retention. Finally, a simple one-pot solution synthesis of Na_2S–NSPS–C nanocomposites for all-solid-state Na–S batteries was successfully demonstrated. The superior performance of the Na_2S–NSPS–C, as compared with manual-mixing electrodes (497 vs 287 mA h g^{-1} in the second cycle), was attributed to nanodomains with intimate contacts derived from the unique solution synthesis. We expect that our results will open new opportunities for the scalable synthesis and discovery of new soft-chemistry-guided superionic conductors for ASSBs.

4. Experimental Section

Material Preparation: For the solution synthesis of $Li_{10}GeP_2S_{12}$, Li_6PS_5Cl, and $Na_{11}Sn_2PS_{12}$ using EDA (98.5%, Sigma-Aldrich) and EDT (98.0%, Sigma-Aldrich), ET (99%, Alfa-Aesar) Li_2S (99.9%, Alfa-Aesar), P_2S_5 (99.9%, Alfa-Aesar), LiCl (99.99%, Alfa-Aesar), GeS_2 (99.9%, American Elements), Na_2S (Sigma-Aldrich), and SnS_2 (99%, MKN) were used as precursor materials. Stoichiometric mixtures were added to the EDA–EDT mixture solvent and stirred at 60 °C for 3 h. For EDT- and ET-$Na_{11}Sn_2PS_{12}$, the solution was stirred at 70 °C. All synthetic procedures were performed under an argon atmosphere. $Li_6PS_5Cl_{0.5}Br_{0.5}$ and Na_3PS_4 used for separating SE layers in all-solid-state Li- and Na-ion cells, respectively, was prepared via ball milling and subsequent HT under an Ar atmosphere. For $Li_6PS_5Cl_{0.5}Br_{0.5}$, after a stoichiometric mixture of Li_2S, P_2S_5, LiCl, and LiBr was ball-milled at 600 rpm for 10 h in a ZrO_2 vial with ZrO_2 balls using a Pulverisette 7PL (Fritsch GmbH), it was subjected to HT at 550 °C for 5 h under an Ar atmosphere. For Na_3PS_4, a stoichiometric mixture of Na_2S and P_2S_5 was ball-milled at 500 rpm for 1 h in a ZrO_2 vial with ZrO_2 balls using a Pulverisette 7PL, followed by HT at 270 °C for 1 h under an Ar atmosphere. $Li_6PS_5Cl_{0.5}Br_{0.5}$ and Na_3PS_4 exhibited ionic conductivities of 4.6×10^{-3} S cm^{-1} and 9.1×10^{-5} S cm^{-1} at 30 °C, respectively. To prepare the Na_2S–NSPS–C nanocomposites, stoichiometric amounts of Na_2S, SnS_2, and P_2S_5 powders were fully dissolved in the EDA–EDT solvent and stirred at 70 °C for 3 h. Super C65 was then added, and the solution was stirred. The target weight ratio of Na_2S/$Na_{11}Sn_2PS_{12}$/super C65 was 30:50:20. The solvent was removed at 150 °C for 3 h under vacuum, and the as-obtained powders were subjected to HT at 700 °C for 12 h under an argon atmosphere. The mixture electrodes were prepared via conventional manual mixing of Na_2S, NSPS (prepared by solid-state synthesis, 0.8 mS cm^{-1}), and super C65, with a weight ratio of 30:50:20.

Material Characterization: Powder XRD patterns were measured using a MiniFlex600 (Rigaku) with Cu-K$_\alpha$ radiation (λ = 1.54056 Å) at 40 kV and 15 mA. The samples were hermetically sealed using a beryllium window. The Raman spectra were collected with an Ar-ion laser beam at an excitation wavelength of 514.5 nm using LabRam Arimis (Horiba

Jobin Yvon). For the cryo-TEM measurements, the samples were loaded onto a lacey Cu grid and mounted on a double-tilt cryo-TEM holder with vacuum transfer (Double tilt LN2 Atmos Defend Holder, Mel-Build) to prevent air exposure of the samples. The cryo-TEM images were obtained using a JEM-2100F (JEOL) at an acceleration voltage of 200 kV. UV–vis spectra were measured using a UV-IR spectrometer (S-4100, SCINCO) and Starna quartz cuvettes with 10 mm path lengths. The TGA data were recorded in the range of room temperature to 700 °C at a scan rate of 5 °C min^{-1} under continuous Ar flow using a Q600 (TA instrument Corp.). Elemental analyses were performed using a Flash 2000 organic elemental analyzer (Thermo Scientific).

Electrochemical Characterization: To extract ionic conductivities of solution-synthesized SEs, two types of symmetric cells were fabricated (Figure S15, Supporting Information): Li/$Li_6PS_5Cl_{0.5}Br_{0.5}$ (200 mg)/Li cell and Li/$Li_6PS_5Cl_{0.5}Br_{0.5}$ (100 mg)/SE (70 mg)/$Li_6PS_5Cl_{0.5}Br_{0.5}$ (100 mg)/Li cell. The ionic conductivities of solution-synthesized $Li_{10}GeP_2S_{12}$, Li_6PS_5Cl, and $Na_{11}Sn_2PS_{12}$ were determined by subtracting the resistance of Li/$Li_6PS_5Cl_{0.5}Br_{0.5}$ (200 mg)/Li cell (=R_{LPSX} + 2R_{int} (Li/LPSX interfacial resistance)) from that of the Li/$Li_6PS_5Cl_{0.5}Br_{0.5}$ (100 mg)/SE (70 mg)/$Li_6PS_5Cl_{0.5}Br_{0.5}$ (100 mg)/Li cells (=R_{LPSX} + 2R_{int} (Li/LPSX interfacial resistance) + R_{SE}).[24] Thus, only the ionic resistances of SE (R_{SE}) could be extracted. The cell resistances were measured by cyclic voltammetry, and confirmed by electrochemical impedance spectroscopy measurements. To assemble the cells, SE powders were placed in a poly(aryl-ether-etherketone) (PEEK) mold (diameter: 13 mm) and pressed under 360 MPa before attaching Li foils on both sides. The TiS_2 composite electrodes were prepared by mixing TiS_2 (99.9%, Sigma-Aldrich) and SEs in a weight ratio of 1:2. $Li_{0.5}In$ (nominal composition) powders prepared by mixing Li powders (FMC Lithium Corp.) and In powder (Sigma-Aldrich, 99%) were used as the counter/reference electrodes. The SE layers were prepared by pelletizing the $Li_6PS_5Cl_{0.5}Br_{0.5}$ powder (150 mg). The as-prepared electrodes (15 mg) and $Li_{0.5}In$ powders (100 mg) were then spread on each side of the SE layer. Finally, the assemblies were pressed at 370 MPa. For the fabrication of all-solid-state Na–S cells, Na_3PS_4 was pelletized and used as the SE layer. Na_3Sn (nominal composition) powders were prepared by mixing Na metal (800 mg) and Sn metal (1376 mg), and used as the counter/reference electrodes, which exhibited an operating voltage of $\approx$0.1 V versus Na/Na$^+$.[9b] After, the Na_2S–NSPS–C and Na_3Sn powders were spread on each side of the Na_3PS_4 layer, the whole assemblies were subjected to pressing at 370 MPa. The mass loading of Na_2S–NSPS–C was 7 mg. All assemblies were carried out in a PEEK mold (diameter: 13 mm) with two Ti rods as the current collectors.

Theoretical Calculations: All DFT calculations were performed using DMol^3 program.[25] The electron exchange-correlation energy was calculated with the generalized gradient approximation and the Perdew–Burke–Ernzerhof functional.[26] The effective core potential was used for core treatment with a basis set of DNP 4.4 level. The convergence criteria for energy, force, and displacement were set as 1.0×10^{-5} Ha, 0.002 Ha Å^{-1}, and 0.005 Å, respectively. The Conductor-like Screening Model solvation model was applied using the dielectric constant of EDA–EDT (10:1 vol) solvent mixture (ε 15.83).[27] To include the dispersion correction of the van der Waals effect, the DFT empirical dispersion correction (DFT-D3) was used.[28] The Brillouin-zone was sampled by a Monkhorst–Pack as a single k-point (Γ-point) for surface model systems. The dipole slab correction was also employed for all slab calculations. To examine the reaction paths, the linear synchronous transit and quadratic synchronous transit methods were used to satisfy the convergence criteria of the RMS force, which was set as 0.003 Ha Å^{-1}.[28] To observe the proton transfer reaction in the EDA–EDT mixture solvent, a DFT model with the explicit solvents was sampled using molecular dynamics (MD) simulation. MD simulation was performed using COMPASS forcefield under the isothermal-isobaric (i.e., *NPT*) ensemble, where *N* is the number of atoms, *P* is the pressure, and *T* is the temperature.[29] The temperature and pressure were maintained at 298 K and atmospheric pressure using a Berendsen thermostat and barostat.[30] The cutoff distance of the van der Waals interaction was set to 12.5 Å, and the electrostatic interactions were calculated using the Ewald summation method with an accuracy of 10^{-5} kcal mol^{-1}. The time step was set to 1 fs, and the total simulation

time was 2 ns. The EDA–EDT mixture solvent was considered to contain 60 EDA molecules and 6 EDT molecules (i.e., 10:1 vol) in a 20 Å cubic box, and the equilibrated density was 0.92 g cc^{-1}. From the last configuration of MD simulation, one EDT molecule and surrounding molecules within 3 Å around the EDT were selected for calculating the energy of proton transfer as EDA–EDT cluster, which contained the 8 EDA molecules and 2 EDT molecules (Figure S5, Supporting Information). To carry out theoretical DFT calculations of the dissolution mechanism on GeS$_2$, a slab model consisting of two atomic layers of GeS$_2$ with the (001) surface of the experimental structure determined by the XRD measurement (Figure S7a, Supporting Information) was employed. The top layer of the model system was relaxed, while the bottom layer was fixed to represent the bulk phase during the optimization calculation. The vacuum region of the slab model was set to ≈30 Å for all slab models to avoid self-interaction errors. When a deprotonated EDT molecule was added near the GeS$_2$ slab region, protonated EDA was also added to the vacuum region for charge balance (Figure S7b, Supporting Information). Note that when two or more protonated EDAs were in the vacuum area, the distances between protonated EDAs were maximized to prevent them from reacting.

Statistical Analysis: Raman spectra shown in Figure 4a were normalized to have identical maximum intensity.

Supporting Information

Supporting Information is available from the Wiley Online Library or from the author.

Conflict of Interest

The authors declare no conflict of interest.

Data Availability Statement

The data that support the findings of this study are available on request from the corresponding author. The data are not publicly available due to privacy or ethical restrictions.

[1] a) L. L. K. David, B. Mitzi, C. E. Murray, M. Copel, A. Afzali, *Nature* **2004**, *428*, 299; b) D. J. Milliron, S. Raoux, R. Shelby, J. Jordan-Sweet, *Nat. Mater.* **2007**, *6*, 352; c) F. Kim, B. Kwon, Y. Eom, J. E. Lee, S. Park, S. Jo, S. H. Park, B. S. Kim, H. J. Im, M. H. Lee, T. S. Min, K. T. Kim, H. G. Chae, W. P. King, J. S. Son, *Nat. Energy* **2018**, *3*, 301.

[2] a) J. Janek, W. G. Zeier, *Nat. Energy* **2016**, *1*, 16141; b) Z. Zhang, Y. Shao, B. Lotsch, Y.-S. Hu, H. Li, J. Janek, L. F. Nazar, C. Nan, J. Maier, M. Armand, L. Chen, *Energy Environ. Sci.* **2018**, *11*, 1945; c) A. Manthiram, X. Yu, S. Wang, *Nat. Rev. Mater.* **2017**, *2*, 16103; d) R. Pfenninger, M. Struzik, I. Garbayo, E. Stilp, J. L. M. Rupp, *Nat. Energy* **2019**, *4*, 475; e) T. Famprikis, P. Canepa, J. A. Dawson, M. S. Islam, C. Masquelier, *Nat. Mater.* **2019**, *18*, 1278; f) R. Chen, Q. Li, X. Yu, L. Chen, H. Li, *Chem. Rev.* **2020**, *120*, 6820; g) Y. H. Xiao, Y. Wang, S. H. Bo, J. C. Kim, L. J. Miara, G. Ceder, *Nat. Rev. Mater.* **2020**, *5*, 105; h) Y. Zhu, Y. Mo, *Angew. Chem., Int. Ed.* **2020**, *59*, 17472; i) J. A. Lewis, F. J. Q. Cortes, Y. Liu, J. C. Miers, A. Verma, B. S. Vishnugopi, J. Tippens, D. Prakash, T. S. Marchese, S. Y. Han, C. Lee, P. P. Shetty, H.-W. Lee, P. Shevchenko, F. D. Carlo, C. Saldana, P. P. Mukherjee, M. T. McDowell, *Nat. Mater.* **2021**, *20*, 503; j) Z. Ning, D. S. Jolly, G. Li, R. D. Meyere, S. D. Pu, Y. Chen, J. Kasemchainan, J. Ihli, C. Gong, B. Liu, D. L. R. Melvin, A. Bonnin, O. Magdysyuk, P. Adamson, G. O. Hartley, C. W. Monroe, T. J. Marrow, P. G. Bruce, *Nat. Mater.* **2021**, *20*, 1121; k) Y. R. Xiao, K. Turcheniuk, A. Narla, A. Y. Song, X. L. Ren, A. Magasinski, A. Jain, S. Huang, H. Lee, G. Yushin, *Nat. Mater.* **2021**, *20*, 984; l) L. Duchene, A. Remhof, H. Hagemann, C. Battaglia, *Energy Storage Mater.* **2020**, *25*, 782; m) H. Kwak, D. Han, J. Lyoo, J. Park, S. H. Jung, Y. Han, G. Kwon, H. Kim, S.-T. Hong, K.-W. Nam, Y. S. Jung, *Adv. Energy Mater.* **2021**, *11*, 2003190; n) Y. Han, S. H. Jung, H. Kwak, S. Jun, H. Kwak, J. H. Lee, S.-T. Hong, Y. S. Jung, *Adv. Energy Mater.* **2021**, *11*, 2100126.

[3] N. Kamaya, K. Homma, Y. Yamakawa, M. Hirayama, R. Kanno, M. Yonemura, T. Kamiyama, Y. Kato, S. Hama, K. Kawamoto, A. Mitsui, *Nat. Mater.* **2011**, *10*, 682.

[4] P. Adeli, J. D. Bazak, K. H. Park, I. Kochetkov, A. Huq, G. R. Goward, L. F. Nazar, *Angew. Chem., Int. Ed.* **2019**, *58*, 8681.

[5] Y.-G. Lee, S. Fujiki, C. Jung, N. Suzuki, N. Yashiro, R. Omoda, D.-S. Ko, T. Shiratsuchi, T. Sugimoto, S. Ryu, J. H. Ku, T. Watanabe, Y. Park, Y. Aihara, D. Im, I. T. Han, *Nat. Energy* **2020**, *5*, 299.

[6] a) K. H. Park, Q. Bai, D. H. Kim, D. Y. Oh, Y. Zhu, Y. Mo, Y. S. Jung, *Adv. Energy Mater.* **2018**, *8*, 1800035; b) A. Miura, N. C. Rosero-Navarro, A. Sakuda, K. Tadanaga, N. H. H. Phuc, A. Matsuda, N. Machida, A. Hayashi, M. Tatsumisago, *Nat. Rev. Chem.* **2019**, *3*, 189.

[7] a) Y. Wang, D. Lu, M. Bowden, P. Z. El Khoury, K. S. Han, Z. D. Deng, J. Xiao, J.-G. Zhang, J. Liu, *Chem. Mater.* **2018**, *30*, 990; b) M. Calpa, N. C. Rosero-Navarro, A. Miura, K. Terai, F. Utsuno, K. Tadanaga, *Chem. Mater.* **2020**, *32*, 9627.

[8] a) E. Rangasamy, Z. Liu, M. Gobet, K. Pilar, G. Sahu, W. Zhou, H. Wu, S. Greenbaum, C. Liang, *J. Am. Chem. Soc.* **2015**, *137*, 1384; b) X. Yao, D. Liu, C. Wang, P. Long, G. Peng, Y.-S. Hu, H. Li, L. Chen, X. Xu, *Nano Lett.* **2016**, *16*, 7148; c) D. Y. Oh, D. H. Kim, S. H. Jung, J.-G. Han, N.-S. Choi, Y. S. Jung, *J. Mater. Chem. A* **2017**, *5*, 20771.

[9] a) K. H. Park, D. Y. Oh, Y. E. Choi, Y. J. Nam, L. Han, J. Y. Kim, H. Xin, F. Lin, S. M. Oh, Y. S. Jung, *Adv. Mater.* **2016**, *28*, 1874; b) A. Banerjee, K. H. Park, J. W. Heo, Y. J. Nam, C. K. Moon, S. M. Oh, S. T. Hong, Y. S. Jung, *Angew. Chem., Int. Ed.* **2016**, *55*, 9634; c) S. Yubuchi, S. Teragawa, K. Aso, K. Tadanaga, A. Hayashi, M. Tatsumisago, *J. Power Sources* **2015**, *293*, 941.

[10] a) D. H. Kim, D. Y. Oh, K. H. Park, Y. E. Choi, Y. J. Nam, H. A. Lee, S. M. Lee, Y. S. Jung, *Nano Lett.* **2017**, *17*, 3013; b) D. H. Kim,

Y.-H. Lee, Y. B. Song, H. Kwak, S.-Y. Lee, Y. S. Jung, *ACS Energy Lett.* **2020**, *5*, 718.

[11] a) F. D. Han, J. Yue, X. L. Fan, T. Gao, C. Luo, Z. H. Ma, L. M. Suo, C. S. Wang, *Nano Lett.* **2016**, *16*, 4521; b) X. Li, J. Liang, X. Yang, K. R. Adair, C. Wang, F. Zhao, X. Sun, *Energy Environ. Sci.* **2020**, *13*, 1429; c) H. Wan, J. P. Mwizerwa, X. Qi, X. Liu, X. Xu, H. Li, Y.-S. Hu, X. Yao, *ACS Nano* **2018**, *12*, 2809.

[12] a) H.-D. Lim, X. Yue, X. Xing, V. Petrova, M. Gonzalez, H. Liu, P. Liu, *J. Mater. Chem. A* **2018**, *6*, 7370; b) S. Teragawa, K. Aso, K. Tadanaga, A. Hayashi, M. Tatsumisago, *J. Mater. Chem. A* **2014**, *2*, 5095; c) H.-D. Lim, H.-K. Lim, X. Xing, B.-S. Lee, H. Liu, C. Coaty, H. Kim, P. Liu, *Adv. Mater. Interfaces* **2018**, *5*, 1701328; d) A. Ito, T. Kimura, A. Sakuda, M. Tatsumisago, A. Hayashi, *J. Sol-Gel Sci. Technol.* **2021**, *101*, 2; e) Y. Subramanian, R. Rajagopal, K.-S. Ryu, *Scr. Mater.* **2021**, *204*, 114129.

[13] H. Michiro, S. Yuji, O. Toshiyuki, M. Hiromu, *Bull. Chem. Soc. Jpn.* **1965**, *38*, 1734.

[14] D. H. Webber, R. L. Brutchey, *J. Am. Chem. Soc.* **2013**, *135*, 15722.

[15] T. Ozturk, E. Ertas, O. Mert, *Chem. Rev.* **2010**, *110*, 3419.

[16] M. Bender, *J. Chem. Educ.* **1952**, *29*, 15.

[17] E. Robinel, B. Carette, M. Ribes, *J. Non-Cryst. Solids* **1983**, *57*, 49.

[18] P. Murria, C. K. Miskin, R. Boyne, L. T. Cain, R. Yerabolu, R. Zhang, E. C. Wegener, J. T. Miller, H. I. Kenttamaa, R. Agrawal, *Inorg. Chem.* **2017**, *56*, 14396.

[19] B. H. Northrop, S. H. Frayne, U. Choudhary, *Polym. Chem.* **2015**, *6*, 3415.

[20] a) M. Duchardt, U. Ruschewitz, S. Adams, S. Dehnen, B. Roling, *Angew. Chem., Int. Ed.* **2018**, *57*, 1351; b) Z. Zhang, E. Ramos, F. Lalere, A. Assoud, K. Kaup, P. Hartman, L. F. Nazar, *Energy Environ. Sci.* **2017**, *11*, 87.

[21] D. Y. Oh, Y. J. Nam, K. H. Park, S. H. Jung, S.-J. Cho, Y. K. Kim, Y.-G. Lee, S.-Y. Lee, Y. S. Jung, *Adv. Energy Mater.* **2015**, *5*, 1500865.

[22] A. C. Ferrari, J. Robertson, *Phys. Rev. B* **2000**, *61*, 14095.

[23] a) Y. Li, Y. Li, A. Pei, K. Yan, Y. Sun, C.-L. Wu, L.-M. Joubert, R. Chin, A. L. Koh, Y. Yu, J. Perrino, B. Butz, S. Chu, Y. Cui, *Science* **2017**, *358*, 506; b) X. Wang, Y. Li, Y. S. Meng, *Joule* **2018**, *2*, 2225; c) Y. B. Song, D. H. Kim, H. Kwak, D. Han, S. Kang, J. H. Lee, S.-M. Bak, K.-W. Nam, H.-W. Lee, Y. S. Jung, *Nano Lett.* **2020**, *6*, 4337.

[24] K. Nagao, Y. Nagata, A. Sakuda, A. Hayashi, M. Deguchi, C. Hotehama, H. Tsukasaki, S. Mori, Y. Orikasa, K. Yamamoto, Y. Uchimoto, M. Tatsumisago, *Sci. Adv.* **2020**, *6*, 7236.

[25] a) B. Delley, *J. Chem. Phys.* **1990**, *92*, 508; b) B. Delley, *J. Chem. Phys.* **2000**, *113*, 7756.

[26] J. P. Perdew, K. Burke, M. Ernzerhof, *Phys. Rev. Lett.* **1996**, *77*, 3865.

[27] a) A. Klamt, G. Schüürmann, *J. Chem. Soc., Perkin Trans.* **1993**, *2*, 799; b) H. Looyenga, *Physica* **1965**, *9*, 501.

[28] a) S. Bell, J. S. Crighton, *J. Chem. Phys.* **1984**, *80*, 2464; b) T. A. Halgren, W. N. Lipscomb, *Chem. Phys. Lett.* **1977**, *49*, 225.

[29] H. Sun, P. Ren, J. R. Fried, *Comput. Theor. Chem.* **1998**, *8*, 229.

[30] A. A. Samoletov, C. P. Dettmann, M. A. J. Chaplain, *J. Stat. Phys.* **2007**, *128*, 1321.